STRUCTURAL BIOLOGY

Structural basis for assembly of TRAPPII complex and specific activation of GTPase Ypt31/32

Chenchen Mi[1]†, Li Zhang[1]†, Guoqiang Huang[1]†, Guangcan Shao[2],
Fan Yang[1], Xin You[1], Meng-Qiu Dong[2], Shan Sun[1]*, Sen-Fang Sui[1,3]*

Transport protein particle (TRAPP) complexes belong to the multiprotein tethering complex and exist in three forms—core TRAPP/TRAPPI, TRAPPII, and TRAPPIII. TRAPPII activates GTPase Ypt31/Ypt32 as the guanine nucleotide exchange factor in the trans-Golgi network to determine the maturation of Golgi cisternae into post-Golgi carriers in yeast. Here, we present cryo-EM structures of yeast TRAPPII in apo and Ypt32-bound states. All the structures show a dimeric architecture assembled by two triangle-shaped monomers, while the monomer in the apo state exhibits both open and closed conformations, and the monomer in the Ypt32-bound form only captures the closed conformation. Located in the interior of the monomer, Ypt32 binds with both core TRAPP/TRAPPI and Trs120 via its nucleotide-binding domain and binds with Trs31 via its hypervariable domain. Combined with functional analysis, the structures provide insights into the assembly of TRAPPII and the mechanism of the specific activation of Ypt31/Ypt32 by TRAPPII.

INTRODUCTION

In eukaryotic cells, vesicles act as the cargo carriers by transporting proteins, lipids, and other materials between various membrane-bound compartments (1). Vesicle transport is a highly sequential process, and each step along the pathway, from the vesicle budding at the donor compartment, via vesicle transporting in cell, to the tethering and fusion with the membrane of the acceptor compartment, is precisely regulated by corresponding factors (2). Tethering refers to the initial interaction between a vesicle and its target membrane (2). It promotes the organization of the soluble N-ethylmaleimide–sensitive factor attachment protein receptor (SNARE) proteins in vesicle fusion (3) and thus is a crucial step in determining the specificity of vesicle trafficking (2). The tethering is highly regulated by the tethering factors, including the conserved guanosine triphosphatases (GTPases) of the Ypt/Rab family, their guanine nucleotide exchange factors (GEFs), and their downstream effectors (4–7). How the different types of tethering factors work together to achieve the overall specificity of the tethering process still remains elusive.

Transport protein particle (TRAPP) complexes belong to the multisubunit tethering complexes and are a highly conserved family of proteins found in all eukaryotes, from yeast to humans. TRAPP complexes from yeast are well studied among this family and have three forms—core TRAPP/TRAPPI, TRAPPII, and TRAPPIII, which function in various vesicle trafficking pathways (8). Core TRAPP/TRAPPI mediates transport from endoplasmic reticulum to cis-Golgi by tethering COPII (coat protein complex II)-coated vesicles (5, 9); TRAPPII interacts with COPI-coated vesicles in mammalian cells and aids in endosome-to-Golgi transport (6, 10, 11); TRAPPIII plays a unique role in autophagy (12). The TRAPP complexes attract particular attention in the vesicle transport because they act as GEFs and play

an essential role in catalyzing nucleotide exchange for Ypt/Rab GTPase. All the three complexes share a core of six different proteins (Bet3, Bet5, Trs20, Trs23, Trs31, and Trs33) that make up core TRAPP/TRAPPI (13). TRAPPII contains four additional proteins (Trs120, Trs130, Trs65, and Tca17) (14), and TRAPPIII has one additional Trs85 (15) in yeast. A proportion of *Aspergillus nidulans* TRAPPIII contains Tca17, as well as TRAPPC11, TRAPPC12, and TRAPPC13 (16), same as metazoan TRAPPIII (table S3) (17, 18). A common core suggests common functions with all complexes acting as GEFs. Core TRAPP/TRAPPI and TRAPPIII are specific to Ypt1 (19–21), whereas TRAPPII activates Ypt31/32 in vivo (11, 22–24). So far, the detailed mechanisms underlying the transition from core TRAPP/TRAPPI and TRAPPIII's GEF activity for Ypt1 to TRAPPII's GEF activity for Ypt31/32 and the functions of the specific subunits of TRAPPII in this transition are insufficiently understood.

Because core TRAPP/TRAPPI is the common element of TRAPP complexes, it has been a subject of various in-depth studies on its structure. A combination of x-ray crystallography and single-particle electron microscopy (EM) showed an elongated rod-shaped structure of core TRAPP/TRAPPI, containing seven subunits (two copies of Bet3 and one copy of each of the other five proteins) arranged side by side (25). The crystal structure of the yeast core TRAPP/TRAPPI core in complex with Ypt1 revealed that four subunits (Bet5p, Trs23, and two Bet3 subunits) interact directly with Ypt1, stabilizing it in an open conformation, facilitating nucleotide exchange (26). *Saccharomyces cerevisiae* TRAPPII is the largest member in the TRAPP family, and its architecture was proposed on the basis of the negatively stained single-particle EM. The data showed that TRAPPII dimerizes into a three-layered, diamond-shaped structure, with two TRAPPI complexes forming the outer layers and the TRAPPII-specific subunits forming the middle layer (27). Core TRAPP/TRAPPI is preserved in both TRAPPII and TRAPPIII, but TRAPPII and TRAPPIII activate different Rab substrates: TRAPPII activates Ypt31/32, and TRAPPIII activates Ypt1 (28). Thus, several questions such as whether TRAPPII uses the same catalytic site as TRAPPIII, and/or how Ypt31/32 is specifically activated by TRAPPII instead of TRAPPI, remain unanswered. Several contradictory results have been reported explaining some of

[1]State Key Laboratory of Membrane Biology, Beijing Advanced Innovation Center for Structural Biology, Beijing Frontier Research Center for Biological Structure, School of Life Sciences, Tsinghua University, Beijing 100084, China. [2]National Institute of Biological Sciences, Beijing 102206, China. [3]Department of Biology, Southern University of Science and Technology, Shenzhen, Guangdong 518055, China.
*Corresponding author. Email: suisf@mail.tsinghua.edu.cn (S.-F.S.); shansun@mail.tsinghua.edu.cn (S.S.)
†These authors contributed equally to this work.

these aspects, but the key fundamental aspect mentioned above remains elusive (*11*, *20*, *29*, *30*).

To address these questions and the fundamental mechanism of TRAPPII in vesicle trafficking, we resolved the structures of the intact TRAPPII and its complex with Ypt32 from *S. cerevisiae* at average resolutions of 3.79 and 3.80 Å, respectively, by single-particle cryo-EM. Combined with biochemistry analyses, structures revealed the detailed interactions between the subunits within TRAPPII and also between TRAPPII and Ypt32, as well as the different conformations of TRAPPII. On the basis of these results, the potential working mechanism for TRAPPII in the vesicle trafficking is discussed.

RESULTS

Overall structure of the TRAPPII complex

The intact TRAPPII complex with an approximate molecular mass of about 1052 kDa was purified from a yeast strain containing FLAG-tagged Trs120. SDS–polyacrylamide gel electrophoresis (PAGE) analysis and mass spectrometry (MS) indicated that all 10 different proteins, including 6 different proteins (Bet5p, Bet3p, Trs20p, Trs23p, Trs31p, and Trs33p) of core TRAPP/TRAPPI and 4 TRAPPII-specific proteins (Tca17, Trs65p, Trs120p, and Trs130p), are present in the purified TRAPPII complex (fig. S1, A and B). One notable improvement is that Tca17, which is one subunit of TRAPPII (*16*, *31*) but was not detected in the previously published structure (*27*), appears to be a stoichiometric component in our sample (fig. S1A). Initial reconstruction led to a structure showing an apparent twofold symmetry (fig. S1, C to E), consistent with the low-resolution negative-stain EM structure indicating TRAPPII as a dimeric complex (*27*) and the negative-stain two-dimensional (2D) averages of TRAPPII from *Aspergillus* (*16*). However, only one-half of this reconstruction displayed clear density and the other half exhibited very poor density, suggesting its heterogeneity (fig. S1E). We used symmetry expansion to deal with this as detailed in Materials and Methods (fig. S1F) (*32*, *33*). Through this strategy, two distinct conformations of monomer were identified, and 3D refinement yielded the closed and open structures at resolutions of 3.79 and 4.18 Å, respectively (figs. S1, F to H, and S2A). The 2:1 ratio of the particles between the closed and open conformation likely suggests that the closed conformation is more stable (fig. S1F). We further assigned each monomer back to its original dimeric particle, resulting in the reconstruction of TRAPPII structure in three different states (fig. S1F). State I contains both monomers in closed conformation, and state III contains both monomers in open conformation (figs. S1F and S2B). State II consists of one monomer in open conformation and the other in closed conformation (figs. S1F and S2B). On the basis of these maps, the atomic models of TRAPPII in open and closed conformations were built (fig. S1, I and J).

The overall structure of TRAPPII looks like a single-arch bridge with about 160 Å height from the side view and has a parallelogram outline from the face view with dimensions of approximately 290 Å by 260 Å (Fig. 1A). The dimeric complex is assembled by two triangle-shaped monomers that are associated with each other through the longest edge composed of Trs120 and Trs65 (Fig. 1A and fig. S2B). Core TRAPP/TRAPPI and Trs130 connected by Tca17 form the middle and shortest edges of the triangle, respectively (Fig. 1A). For monomers in the complex, the major difference between the open conformation and the closed conformation lies in the position of core TRAPP/TRAPPI (Fig. 1D). Superposing Trs120, Trs65, and

Trs130 (fig. S2C) shows that, compared to the open conformation, the core TRAPP/TRAPPI in the closed conformation rotates 16.6° toward the Trs120, pivoting around the core TRAPP/TRAPPI-Trs120 junction, together with a slight turn (8.9°) on its own axis, which leads to a smaller angle between core TRAPP/TRAPPI and Trs120 by about 10° (from 47.3° to 36.9°) (Fig. 1D) and also a larger space of the interior of TRAPPII in the open conformation than in the closed conformation.

Structures of core TRAPP/TRAPPI and Tca17 in TRAPPII

The structure of TRAPPI was well resolved in our EM map, and the complete atomic model was built with all seven subunits assigned accurately (Fig. 1, B and C, and figs. S2A and S3). Core TRAPP/TRAPPI looks like a flat rod about 180 Å long and is formed by the arrangement of Trs33, Bet3-A, Bet5, Trs23, Bet3-B, Trs31, and Trs20 in turn (Fig. 1, B and C), which is in agreement with the previously reported organization of core TRAPP/TRAPPI based on the crystal structures and the low-resolution EM structure (*25*). Most of the structures are well matched upon superimposing with the existing crystal structures, and some loops that were absent in crystal structures are resolved in our maps (fig. S4A). In addition to the interactions between subunits revealed by the crystal structures of subcomplexes, the most notable finding in our cryo-EM structure is that Trs31 extends its long N-terminal loop (residues 25 to 54) first passing through the hole between loop α1-α2 and the C-terminal end of helix α4 of Bet3-B, and then wandering around the surface of Trs20 (fig. S4B), which functions like an arm to hold Trs20 firmly. Compared to human Trs33, yeast Trs33 has extra two β strands and one short α helix (residues 87 to 109) (fig. S4C). The two β strands are docked to the groove formed by helices α3 and α5, and β strand β1 of Bet3-A. The short α helix contacts with the loop α2-α3 of Bet5 (fig. S4C). Together, these interactions could enhance the associations among subunits of core TRAPP/TRAPPI, thus making the whole complex more stable and rigid.

After docking core TRAPP/TRAPPI into the EM map, we can still observe some clear extra density next to Trs33 (fig. S2A). We attributed this density to Tca17. The crystal structure of Tca17 [Protein Data Bank (PDB) ID: 3PR6] fits into the density with high confidence (fig. S2D). Thus, Tca17 is located on the opposite end of the core TRAPP/TRAPPI rod to Trs20 and interacts with Trs33 in the TRAPPII complex (Fig. 1, B and C) (*16*). On the other side, Tca17 also interacts with Trs130, as described in detail below.

Structure of Trs120 in TRAPPII

Because Trs120 and Trs130 have the similar overall domain arrangement, one N-terminal α-solenoid (NTS) domain followed by four immunoglobulin (Ig)–like domains (IgDs) according to the secondary structure predictions (Figs. 2A and 3A), we performed chemical cross-linking of the TRAPPII complex coupled with MS (CXMS) analysis and pull-down experiment to further identify the locations of Trs120 and Trs130. The results of CXMS using both BS[3] (bis(sulfosuccinimidyl)suberate) and DSS (disuccinimidyl suberate) showed cross-links between Trs120 and Trs31, suggesting that Trs120 is close to Trs31 (fig. S5). Moreover, several works have reported the interaction between Trs120 and Trs20 (*16*, *34*). Because the map quality of the N-terminal region (residues 1 to 264) is very poor, we could only build the atomic models of the NTS (residues 264 to 644) and four IgDs (IgD1 to IgD4) of Trs120 (Fig. 2, A and B, and fig. S6A). The NTS domain is a slightly curved spiral consisting of approximately 380 residues arranged into 13 helices (residues
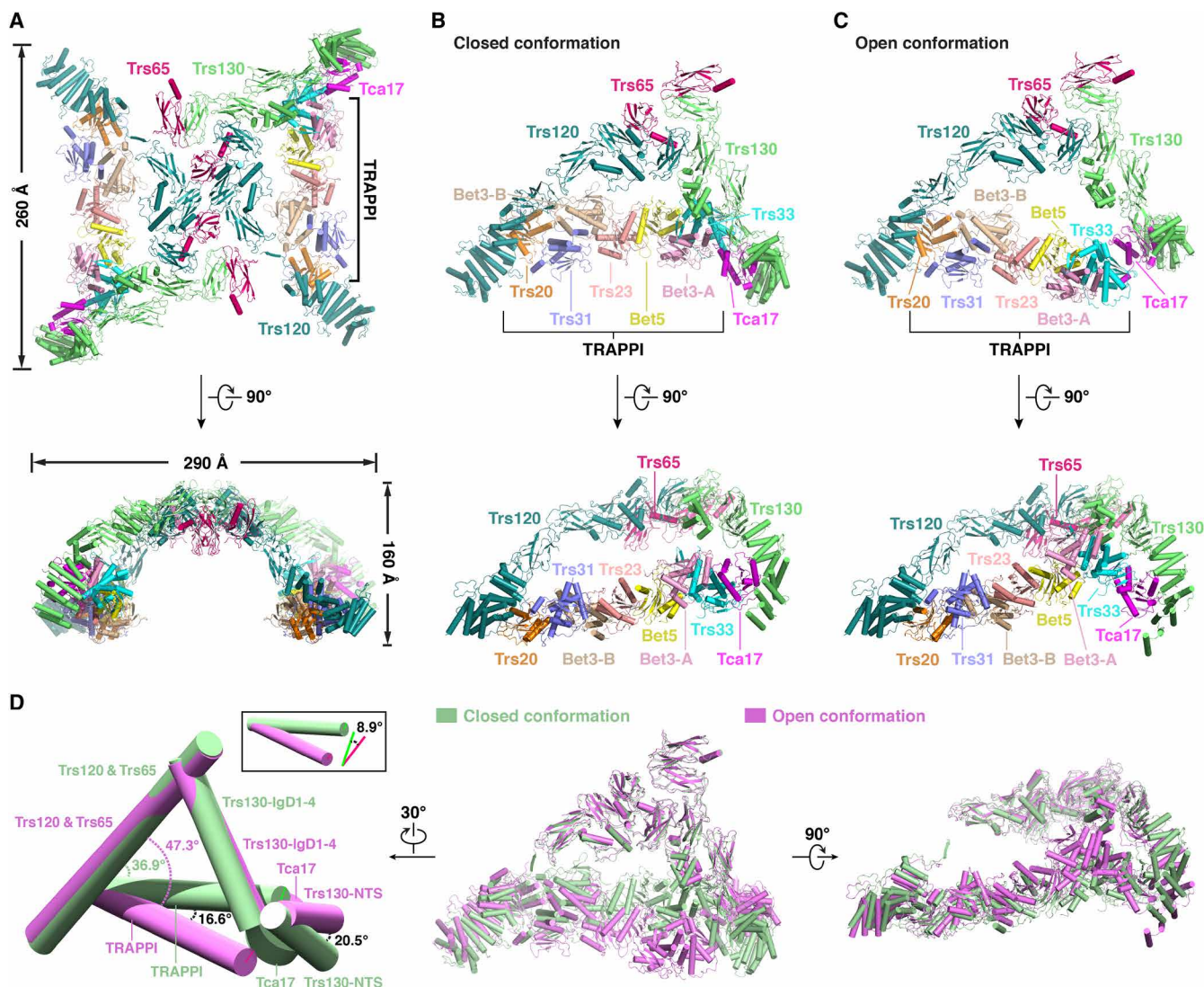
Fig. 1. Structures of the yeast TRAPPII complex. (**A**) Overall structure of the intact yeast TRAPPII in state I. All subunits are color-coded and shown in cartoon representation. (**B**) Structure of the yeast TRAPPII monomer in the closed conformation. All subunits are color-coded and shown in cartoon representation. (**C**) Structure of the yeast TRAPPII monomer in the open conformation. All subunits are color-coded and shown in cartoon representation. (**D**) Structural comparison of the closed (light blue) and open conformations (pink).

264 to 644) and contacts with Trs20 in the core TRAPP/TRAPPI (Figs. 1, B and C, and 2B). IgD2 to IgD4 contribute to the most stable regions of Trs120 (Fig. 2B) and have contacts with both Trs130 and Trs65 (Fig. 1, B and C). Different from the basic structure of IgD, the two helices, α1 in IgD2 and α2 in IgD3, inserted into the loop β2-β3 (loop connecting strands β2 and β3) in IgD2 and loop β6-β7 in IgD3, respectively (Fig. 2C). These decorations in loops lead to two long loops, loop α1-β3 of IgD2 and loop α2-β6 of IgD3, stretching toward the interior of the triangle (Fig. 2C). The large gap between these two loops and core TRAPP/TRAPPI is supposed to be the position of the bound Ypt31/32, which was confirmed by the resolved structure of the TRAPPII-Ypt32 complex described below.

Helices α7, α9, and α11 from Trs120-NTS make extensive interactions with Trs20 (Fig. 2, D and E). In detail, two highly positively charged surfaces of Trs120-NTS contact two acidic patches formed by residues from helix α1 and loops between strands β1 and β2 and

between strands β4 and β5 of Trs20 (Fig. 2D). D46, whose mutation causes spondyloepiphyseal dysplasia tarda (SEDT) in humans (*35*, *36*), is right at one of these two surfaces and contacts with amino acids K527, R528, and K529 from Trs120-NTS (Fig. 2D). Hydrophobic interactions also contribute to the binding between Trs120-NTS and Trs20, as exemplified by the close distances between residues F532, W584, L587, and I591 from Trs120-NTS and I8, P14, F39, I40, L41, A43, and F95 from Trs20 at the interface (Fig. 2E). To further evaluate the physiological relevance of the interaction between Trs120 and Trs20 in vivo, we performed growth assays with truncated Trs120. According to our structure, N-terminal 457 amino acids of Trs120 have no interactions with Trs20. Truncating this region slightly affected the yeast growth at various temperatures (Fig. 2F and fig. S6B). In contrast, deleting the N-terminal 643 amino acids that cover all residues interacting with Trs20 caused yeast death at all temperatures (Fig. 2F and fig. S6B). These results suggest that the interactions between Trs120 and Trs20 are essential
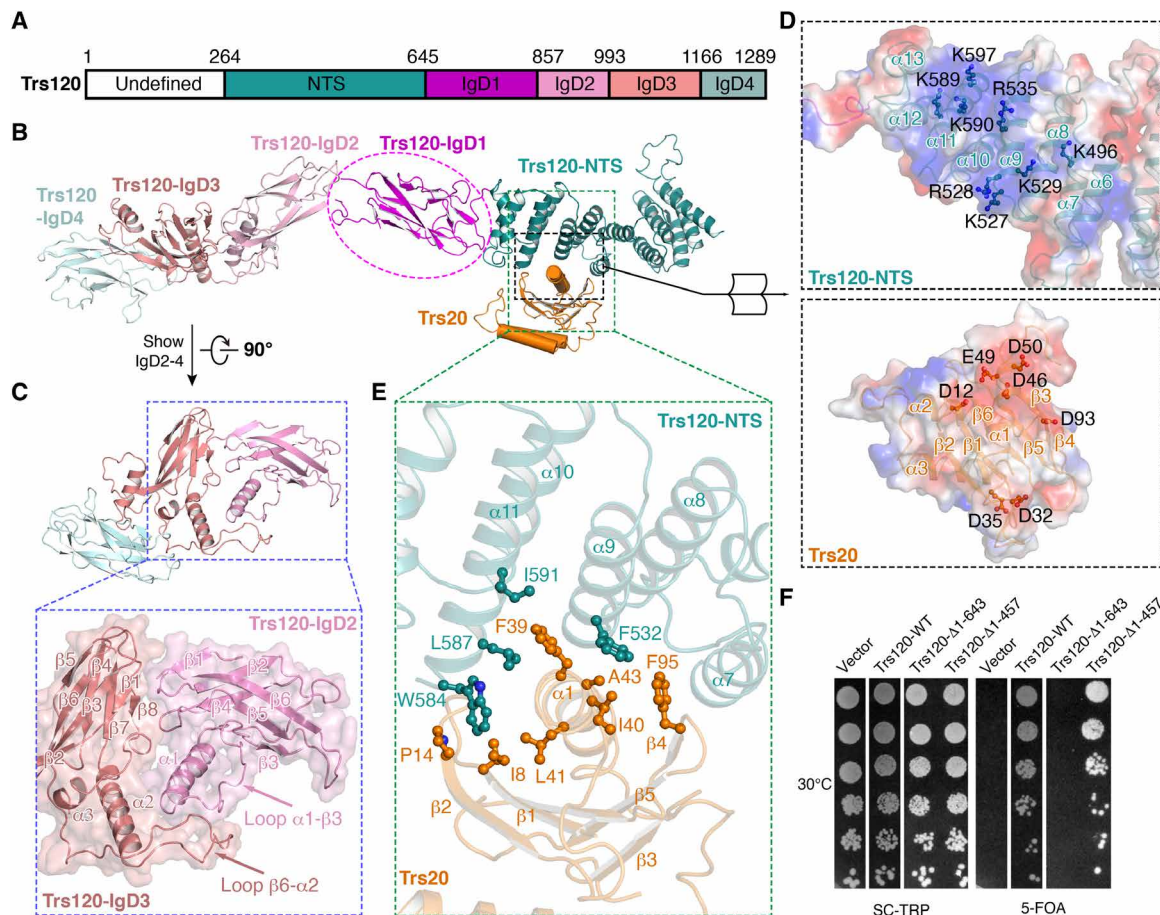
Fig. 2. Structure of Trs120 in TRAPPII. (**A**) Schematic representation of the domain structures of Trs120. Color codes for domains are indicated. Numbers indicate the domain boundaries. (**B**) Overall structure of Trs120. (**C**) Interaction between Trs120-IgD2 and Trs120-IgD3. (**D**) Electrostatic surface representation of the interface between Trs120-NTS and Trs20. The surface potentials are complementary. The amino acid residues involved in the interactions are exhibited as sticks and balls. (**E**) Hydrophobic interactions between Trs120-NTS and Trs20. The amino acid residues involved in the interactions are exhibited as sticks and balls. (**F**) Viability of N-terminal deletion mutants of Trs120 tested by yeast survival and growth assays. Cells were grown at 30°C. Truncating N-terminal 457 amino acids of Trs120 that have no interactions with Trs20 slightly affected the yeast growth, while deleting the N-terminal 643 amino acids that cover all residues interacting with Trs20 caused yeast death. WT, wild type.

for yeast survival, probably by maintaining the proper function of TRAPPII, which is in alignment with the essential role of Trs20 for the TRAPPII function (*34*, *37*).

Structure of Trs130 in TRAPPII

CXMS analysis also identified seven cross-links between Trs130 and Tca17 (fig. S5) (*14*), indicating that the super-helical structure near Tca17 belongs to Trs130. According to the density map at this location, we built an almost complete atomic model of Trs130 except for the N-terminal region (residues 1 to 250) that exhibited no EM density (Fig. 3, A and B, and fig. S6C). The NTS of Trs130 consisting of about 280 residues arranged into 11 helices (residues 250 to 529) is curved more spiral than Trs120-NTS (Figs. 2B and 3B). The four IgD domains are connected sequentially and have similar structures except IgD3. IgD3 is distinguished from others by the insertion of a four-helix bundle into the loop β6-β7 (Fig. 3B). This bundle further bridges IgD1 to IgD3 to stabilize the whole structure of IgD1 to IgD3 (Fig. 3B).

Trs130 exhibits wide contacts with the surrounding proteins. First, similar to the interaction between Trs120-NTS and Trs20, Trs130-NTS contacts with Tca17 (Figs. 1, B and C, and 3B). Helix α1 of Tca17 is wrapped by a barrel formed by helices α5, α7, and α9 of Trs130-NTS and all four β strands of Tca17 (Fig. 3, B and C). In addition, W464 of Trs130-NTS is embedded in a hydrophobic pocket formed by residues L44, I11, and P17 of Tca17, which is similar to the interaction of W584 of Trs120-NTS with L41, I8, and P14 of Trs20 (Figs. 2E and 3D). Second, IgD3 and IgD4 make up an L-shaped structure holding IgD4 of Trs120 (Fig. 3B). Specifically, the loop between strands β4 and β5 of Trs120-IgD4 extended into the hydrophobic interior (Y819 and F835) between the two β sheets of Trs130-IgD3 (Fig. 3E). Third, the loop between strands β4 and β5 of Trs130-IgD4 interacts with the loop between strands β3 and β4 of Trs65-IgD2 (Fig. 3F). Deletion of Trs130-IgD4 in *S. cerevisiae* led to temperature sensitivity (*10*), and further truncating IgD3 resulted in its death, suggesting that IgD3 was more important than IgD4 to the function of TRAPPII (Fig. 3G). Truncating the N-terminal 249 amino acids of Trs130 affected the growth of *S. cerevisiae* slightly in various temperatures (Fig. 3H and fig. S6D), which suggested that this unsolved part also plays some physiological role on the function of TRAPPII.
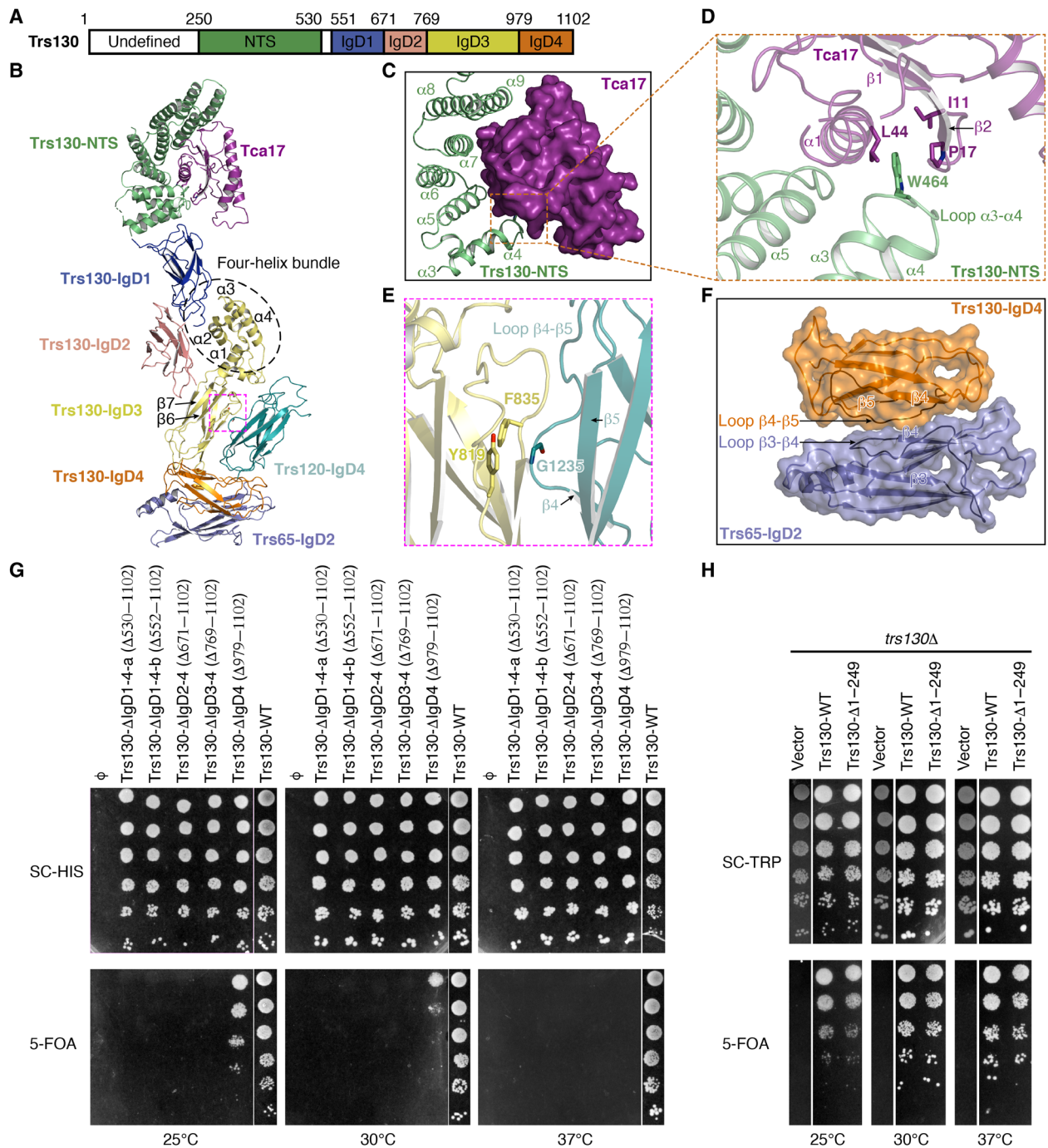
Fig. 3. Structure of Trs130 in TRAPPII. (**A**) Schematic representation of the domain structures of Trs130. Color codes for domains are indicated. Numbers indicate the domain boundaries. (**B**) Overall structure of Trs130. The interacting protein Tca17 and protein domains of Trs120-IgD4 and Trs65-IgD2 are also shown. (**C**) Interaction between Trs130-NTS and Tca17. (**D**) W464 of Trs130-NTS is embedded in a hydrophobic pocket formed by residues L44, I11, and P17 of Tca17. (**E**) Interaction between Trs130-IgD3 and Trs120-IgD4. (**F**) Interaction between the loop β4-β5 of Trs130-IgD4 with the loop β3-β4 of Trs65-IgD2. (**G**) Viability of C-terminal deletion mutants of Trs130 tested by yeast survival and growth assays. (**H**) Viability of N-terminal deletion mutant of Trs130 tested by yeast survival and growth assays.

Structure of Trs65 in TRAPPII

Trs65 is composed of three IgDs according to the structure prediction (fig. S7A). CXMS analysis indicated extensive interactions between Trs65 and Trs120 as well as Trs130 (fig. S5).

Negative-stain images of TRAPPII containing N-terminally His–green fluorescent protein (GFP)–tagged Trs65, which is labeled by anti-His antibody, showed the Y-shaped antibodies flanking TRAPPII, suggesting that the N-terminal IgD1 of Trs65 was located on the lateral side of the TRAPPII complex (fig. S7B). However, its density was too poor to build the atomic model (fig. S7C), likely reflecting its dynamic location due to the long linker between IgD1 and IgD2. Thus, only atomic models of IgD2 and IgD3 of Trs65 were built

(fig. S7C). Detailed analysis of the interactions between Trs65 with surrounding proteins suggests that Trs65 could play a critical role in the dimeric complex formation because it interacts with subunits in both monomers (fig. S7D). In one monomer, besides the interaction between Trs65-IgD2 and Trs130-IgD4 as described above (Fig. 3F and fig. S7D), Trs65-IgD3 also interacts with both IgD3 and IgD4 of Trs120. The interaction between Trs65-IgD3 and Trs120-IgD3 is mainly mediated by hydrophobic residues (fig. S7, D and E). In addition, helix α1 of Trs65-IgD3 binds to a groove formed by strands β3, β6, and β7 and loop β7-β8 of Trs120-IgD4, in which Y487 of Trs65-IgD3 forms π-π interactions with both F1216 and F1279 of Trs120-IgD4 (fig. S7, D and F). Besides these interactions within the same monomer, Trs65-IgD3 is also very close to the IgD2′ and IgD3′ of Trs120′ in the neighboring monomer, suggesting the existence of interactions between them (fig. S7, D and G). Meanwhile, Trs65-IgD2 contacts with Trs120-IgD2′ via the interactions between the loops β3-β4 of Trs65-IgD2 and β2-α1 of Trs120-IgD2′ (fig. S7, D and G). Consistent with the extensive interactions between Trs65-IgD3 and subunits in both monomers, deletion of Trs65-IgD3 from the yeast genome reduced dimer formation, resulting in predominance of monomers (fig. S7H). Similarly, *Drosophila* TRAPPII, which lacks Trs65, is also a monomer (*18*). Together, Trs65 is essential in the stability of TRAPPII in yeast (*14*, *27*).

Structure of the TRAPPII-Ypt32 complex

Furthermore, to explore how TRAPPII acts as a GEF to activate Ypt32, we resolved the structure of the Ypt32-bound TRAPPII complex (fig. S8, A to D). Similar with the Ypt32-free TRAPPII, the TRAPPII-Ypt32 complex is also a dimer assembled by two triangle-shaped monomers (Fig. 4A), but unlike the Ypt32-free TRAPPII in which two distinct conformations of monomer were identified, only one stable conformation of monomer was observed (fig. S8B). The monomer was resolved at the resolution of 3.80 Å, which leads to the accurate assignment of all subunits of TRAPPII and Ypt32 (figs. S8, B to E, and S9, A to C). The subunit arrangement of TRAPPII in the TRAPPII-Ypt32 complex is almost identical to that of Ypt32-free TRAPPII (Fig. 4, A and B). As expected, Ypt32 locates inside the triangle-shaped TRAPPII and at the gap between core TRAPP/TRAPPI and Trs120 (Fig. 4B). Both the nucleotide-binding domain (NBD) and the C-terminal region of Ypt32 contribute to interactions with TRAPPII (Fig. 4B).

For interactions between NBD of Ypt32 and TRAPPII, there are three contact sites between Ypt32's NBD and TRAPPII (Fig. 4B). One binding site lies at the interface between NBD of Ypt32 and core TRAPP/TRAPPI (Fig. 4B), which is very similar with the interaction between core TRAPP/TRAPPI and Ypt1 (*26*). The most notable observation is that two additional binding sites are formed between NBD of Ypt32 and the TRAPPII-specific component Trs120. We name them TRAPPII-specific binding sites 1 and 2, respectively (Fig. 4B).

For the TRAPPII-specific binding site 1, the loop (residues N694 to K703) between strands β1 and β2 of Trs120-IgD1, namely, Trs120-IgD1-Loop, precisely fits in the groove formed by strand β5 and helices α4 and α5 of Ypt32 through both hydrophobic and polar interactions (Fig. 4, C to E, and fig. S9D). The C-terminal part of the Trs120-IgD1-Loop including four hydrophobic residues (V698, F699, P701, and F702) is nestled in a hydrophobic surface constituted by A120, A145, M146, L151, F152, A166, and A173 of Ypt32 (Fig. 4, D and E). Three hydrogen bonds (H-bonds) between

Trs120-IgD1-Loop and helix α5 of Ypt32 are observed including the interactions of Q696/Trs120 and N159/Ypt32, Q696/Trs120 and N162/Ypt32, and N700/Trs120 and E169/Ypt32 (Fig. 4E). In addition, the main-chain amide group of N694 and carbonyl oxygen (C=O) of F699 from Trs120-IgD1-Loop make H-bonds with the side group of T138 and the main-chain amide group of F152 from Ypt32, respectively (Fig. 4E). Moreover, the positively charged Ypt32-K142 forms one cation-π interaction with the aromatic group of Trs120-F699 (Fig. 4E). Sequence alignment of Ypt31/32 and Trs120 from different species indicates that the hydrophobic residues involved in the interaction between Trs120-IgD1-Loop and Ypt32 are more conserved than the charged and polar residues, suggesting that the hydrophobic contacts may play a dominant role in this interaction (fig. S10).

For the TRAPPII-specific binding site 2, a long loop between helix α2 and strand β6 of Trs120-IgD3 (Trs120-IgD3-Loop), which stretches toward the interior of the triangle-shaped TRAPPII, also interacts with Ypt32 (Fig. 4, B and F). Arg[134] in Ypt32 contributes two H-bonds at this interface. One is formed by the guanidinium group of Arg[134] with the main-chain C=O of Gln[1103] in Trs120, and the other is between the main-chain C=O of Arg[134] and the main-chain amide groups of Gln[1106] in Trs120. In addition, potential hydrophobic interaction occurs between Pro[137] in Ypt32 and Ile[1105] in Trs120 (Fig. 4F).

When we examined the conformational change induced by the binding of Ypt32 to TRAPPII by superposing the TRAPPII-Ypt32 complex with the open and closed conformations of Ypt32-free TRAPPII, the results indicate that the Ypt32-bound TRAPPII exhibits the closed conformation (Fig. 4G). Moreover, binding with Ypt32 brings core TRAPP/TRAPPI and Trs120 closer (Fig. 4, G and H), because Ypt32 contacts with both of them (Fig. 4B). Therefore, core TRAPP/TRAPPI moved slightly toward Trs120, leading to a more compact conformation of the TRAPPII-Ypt32 complex (Fig. 4, G and H).

For interactions between the C-terminal region of Ypt32 and TRAPPII, in our map of the TRAPPII-Ypt32 complex, the density for the C-terminal region including the hypervariable domain (HVD) of Ypt32 could be observed, although only partial sequence (186 to 200) was modeled with polyalanine due to the low resolution. The structure shows that this C-terminal region of Ypt32 extends as a rope to attach to the surface of Trs31 (Fig. 5A). CXMS analysis further indicated the cross-linking between Lys[211] of Ypt32 and Lys[168] of Trs31 pairs (fig. S8F). Meanwhile, the Ypt1 C-terminal region connecting with Trs31 was observed in the yeast TRAPPIII-Ypt1 complex (*38*). To further investigate the interaction between HVD and TRAPPII, we constructed several C-terminally truncated Ypt32 mutants and tested their binding abilities with TRAPPII (Fig. 5, B to H). Deleting the last 10 (Ypt32 1 to 212) or 15 (Ypt32 1 to 207) residues at the C-terminal region of Ypt32, the protein could still bind to TRAPPII, and the binding ability was similar to that of wild-type Ypt32 (Fig. 5, G and H). However, further deleting six more residues (Ypt32 1 to 200) led to a significant decrease of the binding ability (Fig. 5F). After deleting the whole HVD (Ypt32 1 to 187), the protein completely lost its ability to bind with TRAPPII (Fig. 5E). These results indicate that HVD plays an essential role in the binding of Ypt32 with TRAPPII, and the conserved residues 201 to 207 of HVD are critical to this interaction. This result is consistent with an earlier study showing that conserved residues of the Ypt31/32 HVD are important for TRAPPII-mediated nucleotide exchange (*39*).
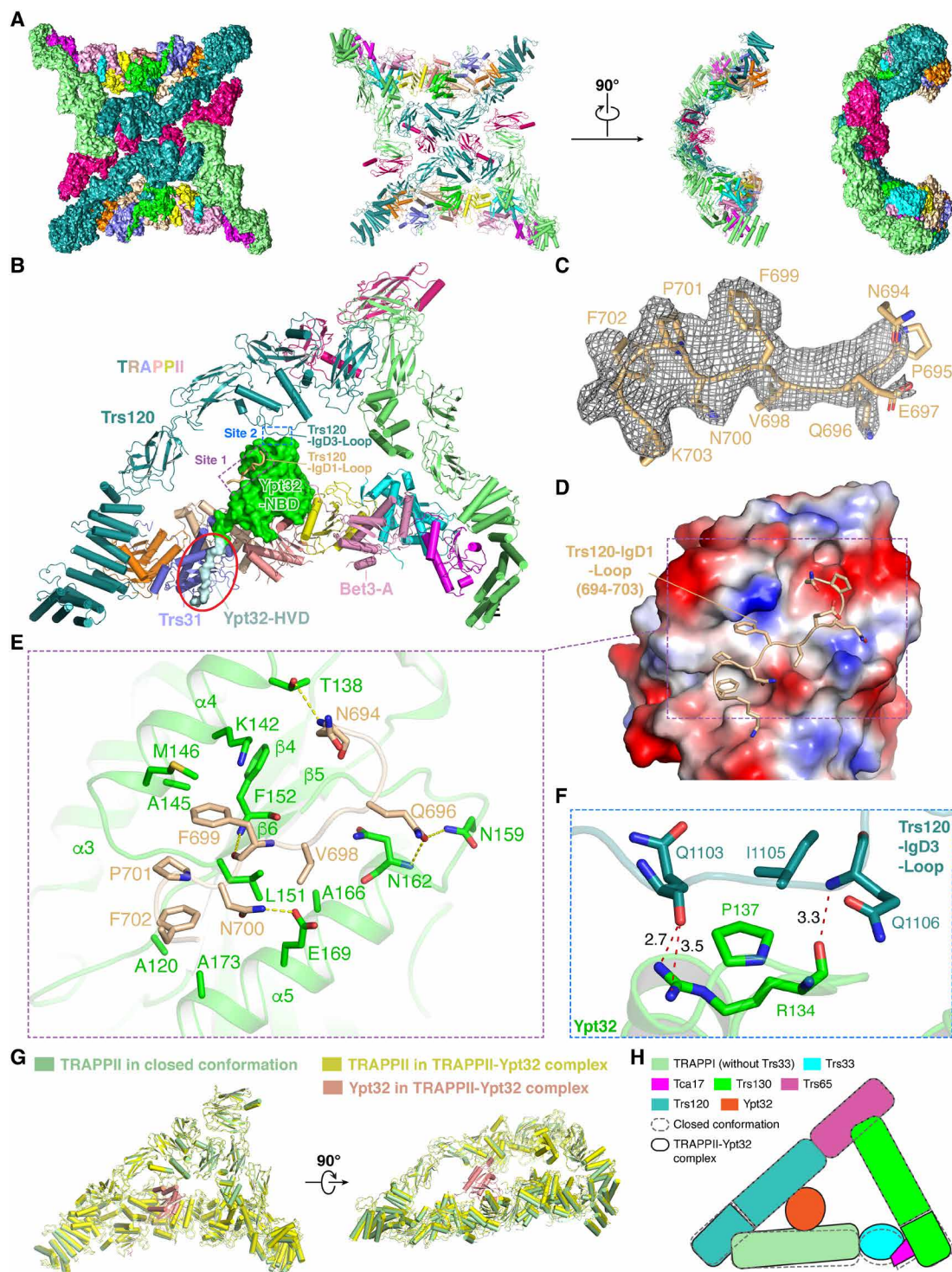
Fig. 4. Structure of the TRAPPII-Ypt32 complex. (**A**) Density map and atomic model of the intact dimeric TRAPPII-Ypt32 complex. All subunits are color-coded, and the coloring scheme is the same as in Fig. 1A. Ypt32 is colored by green. Two perpendicular views are shown. (**B**) Overall structure of the TRAPPII-Ypt32 monomer. TRAPPII is shown in cartoon representation, and Ypt32 is displayed in surface representation. TRAPPII-specific binding sites 1 and 2 are boxed by dashed lines. Red circle indicates the interaction between the C-terminal region of Ypt32 (186 to 200) and Trs31. This region is zoomed in Fig. 5A. (**C**) Cryo-EM densities (mesh) for Trs120-IgD1-Loop (sticks). (**D**) Trs120-IgD1-Loop is embedded in one groove of Ypt32. Ypt32 is displayed in the electrostatic surface representation. (**E**) Interactions between Trs120-IgD1-Loop and Ypt32. The amino acid residues involved in the interactions are exhibited as sticks. (**F**) Interactions between Trs120-IgD3-Loop and Ypt32. The amino acid residues involved in the interactions are exhibited as sticks. (**G**) Structural comparison of the Ypt32-bound TRAPPII and the closed conformation of the Ypt32-free TRAPPII. (**H**) Schematic diagram showing the conformational change between the Ypt32-bound TRAPPII and the closed conformation of the Ypt32-free TRAPPII.
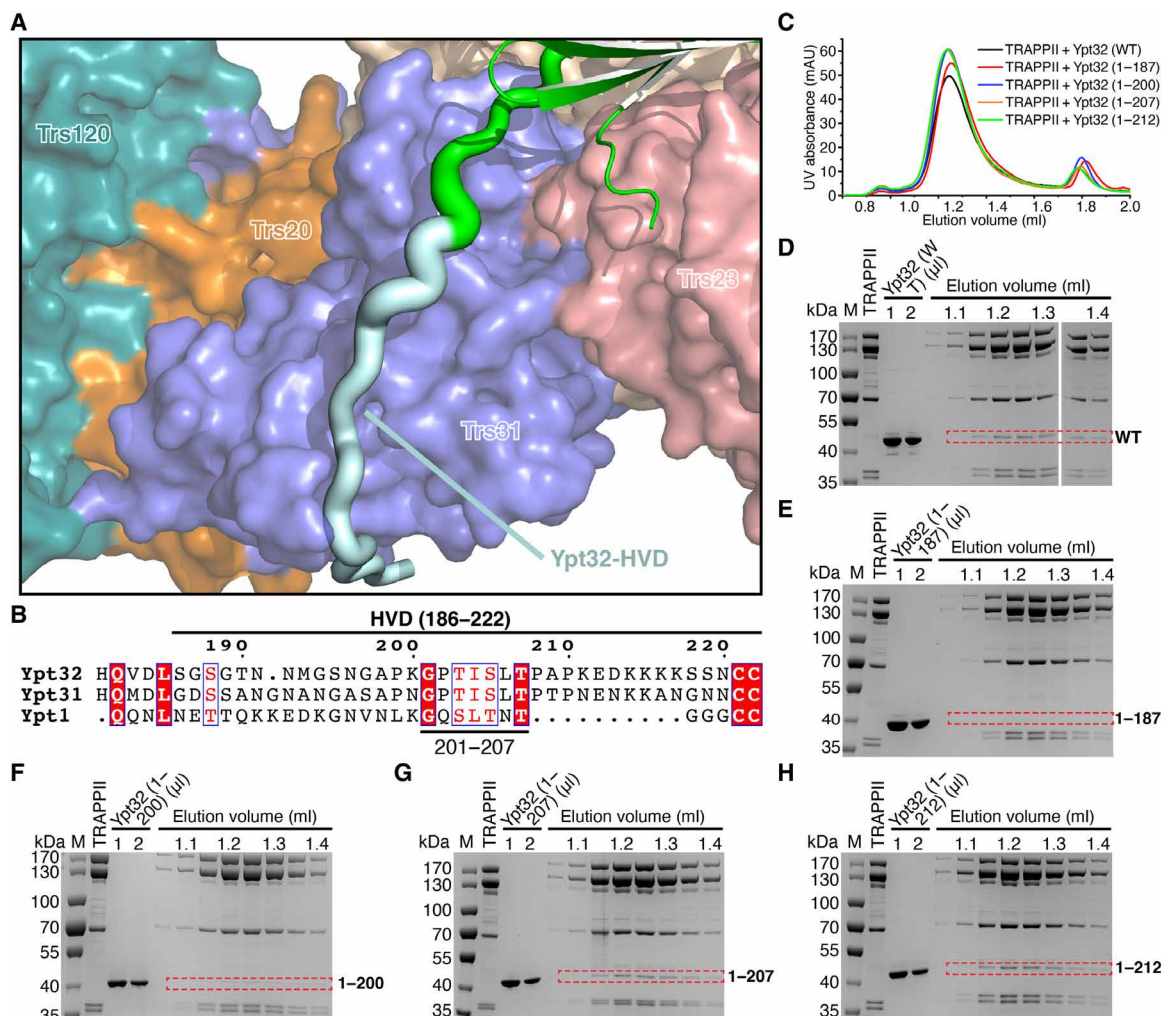
Fig. 5. Attachment of the C-terminal region of Ypt32 to Trs31. (**A**) Zoomed view of the interaction between the C-terminal region of Ypt32 to Trs31. (**B**) Sequence alignment of the C-terminal region of Ypt32, Ypt31, and Ypt1 from *S. cerevisiae*. (**C**) Fast protein liquid chromatography (FPLC) curves of the mixtures of TRAPPII incubated with indicated C-terminal deletion mutants of Ypt32. UV, ultraviolet; mAU, milli-absorbance unit. (**D** to **H**) Peak fractions of the FPLCs were analyzed by SDS-PAGE. Purified wild-type and truncated Ypt32 proteins are displayed in different amounts (1 and 2 μl) in two lanes on the gels. The position of Ypt32 protein in FPLC fractions is marked by a red dotted box.

Mechanism of Ypt32 activation

To investigate the role of interactions of the TRAPPII-specific loops with Ypt32, we compared the structures of Ypt32 in the TRAPPII-Ypt32 complex, in the guanosine diphosphate (GDP)–bound state (PDB: 3RWO) (*40*) and in the GppNHp (guanosine-5′-(βγ-imino) triphosphate) [a nonhydrolyzable analog of guanosine triphosphate (GTP)]–bound state (PDB: 3RWM) (*40*) by superposing them (Fig. 6A). We found that the presence of Trs120-IgD1-Loop causes steric clashes of N694, Q696, and V698 from Trs120-IgD1-Loop with T138, N162, K165, and E169 on helices α4 and α5 from Ypt32 in the GDP-bound state as evident by the overclose distances between them (Fig. 6B, inset), thus pushing helices α4 and α5 outward to overcome the steric hindrances (Fig. 6B). Because helix α5 is connected to the Ser-Ala-Leu (SAL) motif (residues 156 to 158) that is involved in the interaction with the guanine base (*26*, *41*, *42*), its movement causes the shift in SAL motif position. In addition, the movement of helix α4 changes the position of the loop α4-β5, which is also affected by binding with Trs120-IgD3-Loop (Fig. 6B). Because

the loop α4-β5 also interacts with the SAL motif (Fig. 6B), its movement also leads to the change of SAL position. Thus, all of these interactions drive the relocation of the SAL motif (Fig. 6B). In detail, Ala[157] of Ypt32 moves toward to the nucleotide-binding pocket, leading to an overclose distance between Ala[157] and the guanosine base, which could interfere with the nucleotide binding (Fig. 6B). Moreover, L158, which stabilizes the guanosine base via the hydrophobic interaction with the guanine ring in the GDP-bound state (*40*, *43*), moves away from the binding pocket and no longer interacts with the guanosine base of the ligand (Fig. 6B). All these results suggest that binding with Trs120 loops induces a conformational change affecting the position of the SAL motif of Ypt32, which facilitates GDP release.

Along with the movement of the SAL motif detailed above, notable differences also occur in switch I and II motifs upon TRAPPII binding (Fig. 6, C and D). Because of the steric clash with the C terminus of Bet3-A, switch I motif (residues 34 to 48, SWI) of the TRAPPII-bound Ypt32 moves away from the nucleotide-binding
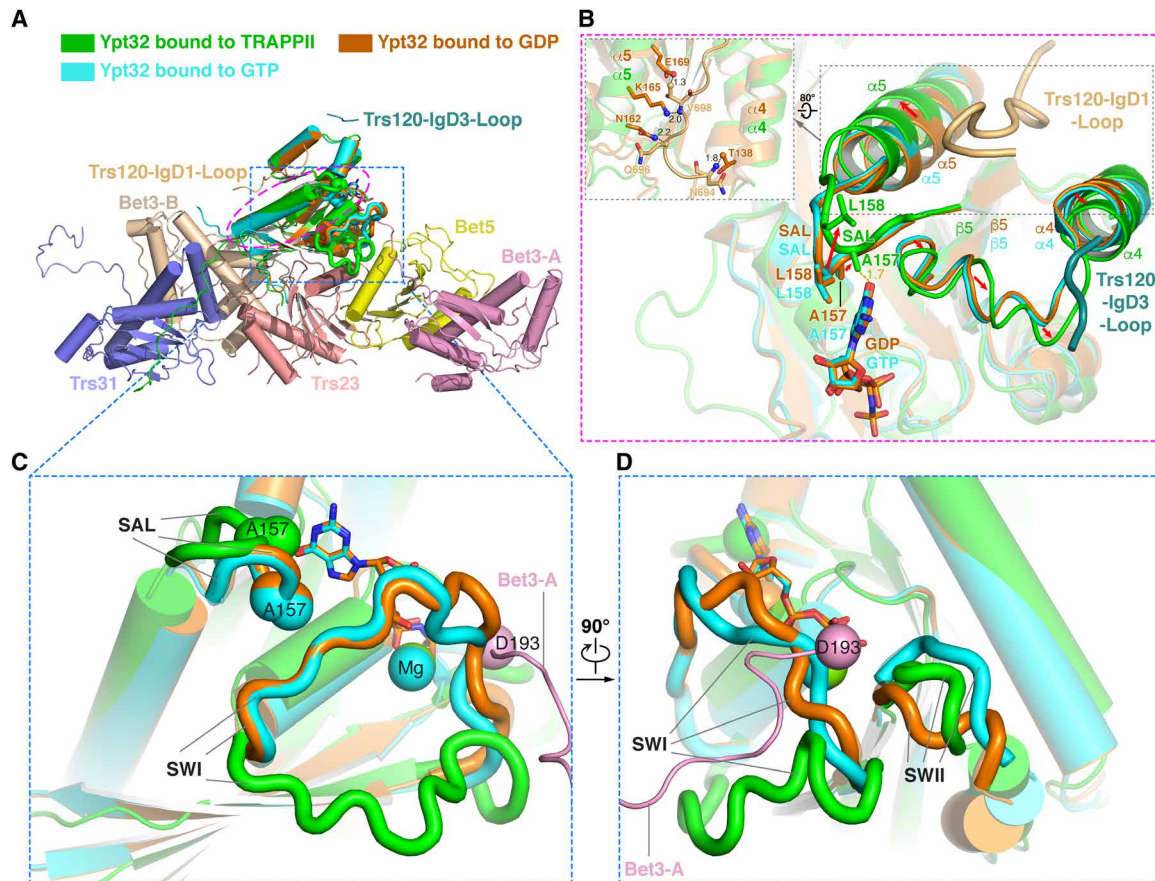
Fig. 6. Mechanism of Ypt32 activation. (A) Structural comparison of Ypt32 bound to TRAPPII, to GDP (PDB: 3RWO), and to GTP (GppNHp; PDB: 3RWM). **(B)** Binding with Trs120 loops causes the movement of helices α4 and α5, and loop α4-β5 of Ypt32, and the relocation of residues in the SAL motif (red arrows). Inset: Steric clashes are observed between N694, Q696, and V698 from Trs120-IgD1-Loop and T138, N162, K165, and E169 on helices α4 and α5 from Ypt32 in the GDP-bound state, thus pushing helices α4 and α5 of Ypt32 outward to overcome the steric hindrances. The numbers near the lines indicate the distances (Å). **(C)** Different positions of SAL and SWI motifs. The residue A157 in the SAL motif, the last residue D193 at the C terminus of Bet3-A, and the magnesium cation are presented as spheres. **(D)** Different positions of SWI and SWII motifs.

pocket, which opens the nucleotide-binding pocket in a favorable conformation for the nucleotide release (Fig. 6, C and D). Additional difference occurs on the switch II motif (residues 68 to 86, SWII), which adopts an intermediate position between SWII positions seen in the GTP- and GDP-bound states (Fig. 6D). All of these structural features indicate that Ypt32 in the TRAPPII-Ypt32 complex is in open conformation, which is consistent with the fact that no nucleotide density was observed in the map of the TRAPPII-Ypt32 complex.

From our structure of the TRAPPII-Ypt32 complex, Ypt32 makes contacts with core TRAPP/TRAPPI in TRAPPII, in a very similar fashion to that of Ypt1 and core TRAPP/TRAPPI. However, previous studies have shown that core TRAPP/TRAPPI alone could not activate Ypt31/32 both in vitro and in vivo (*11*, *26*, *28*). This phenomenon suggested that interaction of Ypt1 with core TRAPP/TRAPPI is sufficient for Ypt1 activation, but interaction of Ypt31/32 with core TRAPP/TRAPPI is not enough to make core TRAPP/TRAPPI activate Ypt31/32. To uncover the possible reason behind the different GEF activity between core TRAPP/TRAPPI for Ypt1 and TRAPPII for Ypt32, we analyzed several related structures. In the cytosol, the inactive Ypt GTPase is bound with a GDP dissociation inhibitor (GDI) (*41*, *44*). Once the GDI-bound Ypt is recruited to the membrane

and interacts with GEF, GDP is released, followed by GTP loading. Thus, we compared the structure of Ypt1 in the GDI-bound state (PDB: 2BCG) (*45*) with its structure in the core TRAPP/TRAPPI-Ypt1 complex (PDB: 3CUE) (*26*). We also compared the structure of Ypt31 in the GDI-bound state (PDB: 3CPJ) (*46*) with the Ypt32's structure in the TRAPPII-Ypt32 complex, because only the structure of the Ypt31-GDI complex has been resolved and Ypt31 shares more than 80% sequence identity with Ypt32 (Fig. 7A). We found that the loop β2-β3 of Ypt1 moves toward the core TRAPP/TRAPPI upon binding to this complex (Fig. 7B), whereas the equivalent loop of Ypt32 does not change at all upon binding to TRAPPII (Fig. 7C). In Ypt1, such a change drives the movement of helix α5 via the polar interaction between D53 in the loop β2-β3 and K170 in helix α5, which further causes the relocation of the SAL motif to facilitate the nucleotide release (Fig. 7B). Similar conformational change of Ypt1 was observed when we compared the structure of Ypt1 in the GDI-bound state (PDB: 2BCG) (*45*) with its structure in the TRAPPIII-Ypt1 complex (PDB: 7KMT) (*38*). Different from Ypt1, the loop β2-β3 of Ypt32 remains unchanged upon binding to core TRAPP/TRAPPI of TRAPPII (Fig. 7C). However, binding of TRAPPII to Ypt32 leads to the repositioning of the SAL motif similar to core TRAPP/TRAPPI-Ypt1 (Fig. 7C). This is found to be due to Trs120,

Fig. 7. Model of TRAPPII-mediated Ypt32 activation. (**A**) Sequence alignment of Ypt31 and Ypt32 from yeast. (**B**) Structural comparison of Ypt1 bound to GDI (PDB: 2BCG) and to TRAPPI (PDB: 3CUE). (**C**) Structural comparison of Ypt31 bound to GDI (PDB: 3CPJ) and Ypt32 bound to TRAPPII. (**D**) First, TRAPPII is recruited onto the trans-Golgi network (I). Then, direct recognition of the Ypt32 HVD by TRAPPII ensures the specific interaction between Ypt32 and TRAPPII. The residues of G201-T207 (red) are indispensable for this binding. As the space of the interior of TRAPPII in the open conformation is larger than that in the closed conformation, Ypt32 may be more likely to bind to the open conformation (II). Upon binding to Ypt32, the open conformation changes to the closed conformation (III). Along with this transition, Ypt32 interacts with Trs120 (III), which is coordinated with the interaction of Ypt32 with core TRAPP/TRAPPI to make Ypt32 adapt to a favorable microenvironment for the nucleotide release (IV).

the TRAPPII-specific subunit, which plays a role in the relocation of Ypt32's SAL motif. As shown in Fig. 6B, binding with Trs120-IgD1-Loop causes the conformational change of Ypt32's SAL motif to adapt to a favorable microenvironment for nucleotide release. Thus, these results may explain why core TRAPP/TRAPPI alone is incapable of activating Ypt32, and reveal the critical role of Trs120 in TRAPPII's activation of Ypt32.

DISCUSSION

In this work, we resolved structures of yeast TRAPPII in apo and Ypt32-bound states. These structures reveal the positions and the structures of the four TRAPPII-specific subunits, Trs120, Trs130, Tca17, and Trs65. According to our structure, the TRAPPII monomer resembles a triangle, and the three edges are formed by core TRAPP/TRAPPI, Trs120, and Trs130, respectively. Such an assembly way suggests the importance of Trs120 and Trs130 for the integrity and stability of TRAPPII, which is consistent with the lethality resulting from loss of *Trs120* or *Trs130* in yeast (*47*). The other two TRAPPII-specific subunits, Tca17 and Trs65, are not essential to yeast cell viability (*30*, *47*). In our structure, Tca17 is located at one end of the core TRAPP/TRAPPI rod and stabilizes the interaction of TRAPPII-specific subunit Trs130 with the core TRAPP/TRAPPI subunit Trs33. Previous study indicated that loss of *Tca17* does not abolish the formation of TRAPPII but reduces its assembly by approximately 40% (*31*). Thus, it is possible that, without Tca17, TRAPPII could still be assembled, as evidenced by the observation of the structure of TRAPPII lacking Tca17 reported by Walz and colleagues (*27*). It should be noted that Tca17 is essential in *A. nidulans* and lethality rescue analysis tracked down this essentiality to its role in TRAPPII (*16*). However, TRAPPII is assembled in *Tca17*-deleted mutants, meaning that *Tca17*-deleted TRAPPII in *A. nidulans* is not functional (*16*). According to our structure and others' reports (*16*, *27*), yeast TRAPPII is a dimer and Trs65 is essential to the formation of TRAPPII dimer. Although Trs65 is not essential for viability (*30*, *47*), yeast cells with *Trs65* deletion have low levels of Trs130 protein, are defective in the GEF activity of TRAPPII and the intracellular distribution of Ypt31/32, and are sensitive to three agents that induce oxidative stress (*30*, *48–50*). Therefore, it is reasonable to deduce that the monomer of TRAPPII may be able to function in the cells, allowing cells to grow under normal conditions. However, TRAPPII dimer might be more stable and efficient than the monomer, which is important for the cells to resist stresses.

The monomer in the Ypt32-free TRAPPII exhibits both open and closed conformations, while the monomer in the Ypt32-bound TRAPPII only captures the closed conformation. According to the structures, the space of the interior of TRAPPII in the open conformation is larger than that in the closed conformation and the binding site for Ypt32 is more exposed in the open conformation; therefore, the open conformation could possibly accommodate the Ypt32 more favorably than the closed conformation (Fig. 1, B to D). Then, the flexible nature of TRAPPII varying between open and closed conformations leads to the closed conformation of Ypt32-bound TRAPPII. The switch from the open conformation to the closed conformation causes Ypt32 to move closer to Trs120 and eventually interact with Trs120, which induces the conformational change of Ypt32 for activation (Figs. 6 and 7C).

According to the different conformations of Ypt32-free TRAPPII and Ypt32-bound TRAPPII and the previously reported steric gating

mechanism for substrate selection (*39*), we proposed a hybrid model of TRAPPII-mediated Ypt32 activation (Fig. 7D). First, TRAPPII is recruited as a whole onto the trans-Golgi network by anion charge and other factors, such as the regulatory GTPase Arf1 (*28*, *51*). Then, direct recognition of the Ypt32 HVD by TRAPPII, together with steric exclusion of the shorter Ypt1 HVD, ensures the specific interaction between Ypt32 and TRAPPII (*39*). As discussed above, the open conformation could be readier to bind Ypt32 than the closed conformation (Fig. 1, B to D). However, binding of Ypt32 to TRAPPII in the open conformation appears unstable, as suggested by the fact that only the closed conformation is observed in the TRAPPII-Ypt32 complex (Fig. 4G and fig. S8B). Thus, in the following step, the open conformation changes to the closed conformation upon binding to Ypt32. Along with this transition, Ypt32 interacts with Trs120, which induces the conformational change of the SAL motif. The interaction of Ypt32 with the core TRAPP/TRAPPI leads to the relocation of SWI and SWII. All of these structural changes make Ypt32 adapt to a favorable micro-environment for the nucleotide release.

MATERIALS AND METHODS
Clones and plasmids
Strains with C-terminal Flag-tagged Trs120 or with gene sequence deletion or truncation were constructed by lithium acetate method (*52*). The genome of *S. cerevisiae* cells was used as the polymerase chain reaction (PCR) template for all plasmid construction. Gene sequence of Trs20 and residues 406 to 644 of Trs120 were optimized for exogenous expression of *Escherichia coli*.

Purification of TRAPPII
The Trs120-3xFLAG–tagged *S. cerevisiae* (44 liters) were grown in YPD (yeast extract peptone dextrose) medium at 30°C overnight until an OD_{600} (optical density at 600 nm) reached 5 to 6. The cells were pelleted by centrifugation and resuspended using the lysis buffer [20 mM Hepes-NaOH (pH 7.4), 150 mM NaCl, 10% glycerol, 1% CHAPS, 1 mM EDTA, 2 mM dithiothreitol (DTT), 1 mM phenylmethylsulfonyl fluoride (PMSF)] supplemented with a protease inhibitor cocktail (Roche). The cell pellets were frozen by liquid nitrogen and then lysed with Freezer Mill 6875 (SPEX CertiPrep). The lysate was centrifuged at 142,400*g* for 40 min using a Type 45 Ti rotor (Beckman). All supernatants were incubated with anti-Flag affinity resin (Sigma-Aldrich) at 4°C for 2 hours. The resin was then washed by the washing buffer [20 mM Hepes-NaOH (pH 7.4), 300 mM NaCl, 10% glycerol, 0.1% CHAPS, 1 mM EDTA, 2 mM DTT] and eluted with the washing buffer supplemented with Flag peptide (0.1 mg/ml; Sigma-Aldrich). The eluate was concentrated and applied to Superose 6 Increase 3.2/300 (GE Healthcare) equilibrated with the sample buffer [20 mM Hepes-NaOH (pH 7.4), 150 mM NaCl, 2 mM DTT, 0.05% digitonin]. The peak fractions were analyzed by SDS-PAGE and the MS analysis.

Preparation of the TRAPPII-Ypt32 complex
E. coli BL21 (DE3) transformed by His-sumo-Ypt32 plasmid were grown at 37°C and then induced by 0.5 mM isopropyl-β-D-thiogalactopyranoside (IPTG) at 16°C overnight. The cells were collected by centrifugation at 5000*g* for 10 min using the F8-6 × 1000y rotor (Thermo Fisher Scientific), washed once with double-distilled H_2O, and resuspended in the basic buffer [20 mM Hepes-NaOH

(pH 7.4), 300 mM NaCl, 5% glycerol] with 1 mM PMSF. Then, the cells were homogenized twice at 4°C using French Press (EmulsiFlex-C3, Avestin) at 1000 bar. The lysate was centrifuged at 18,000g for 30 min using the JA25.50 rotor (Beckman). The supernatants were incubated with Ni-beads (GE Healthcare) at 4°C for 1 hour. Then, the beads were washed by the basic buffer with 20 mM imidazole and eluted with the basic buffer supplemented with 300 mM imidazole (Sigma-Aldrich). The elute was then applied to Superdex 200 Increase 3.2/300 (GE Healthcare) equilibrated with the incubation buffer [20 mM Hepes-NaOH (pH 7.4), 150 mM NaCl, 5% glycerol, 2 mM DTT] with 20 mM EDTA and 0.05% digitonin. The TRAPPII complex was changed into the same buffer by gel filtration. To prepare the TRAPPII-Ypt32 complex, the TRAPPII complex and his-sumo-Ypt32 were mixed in a molar ratio of 1:1.5 at 4°C for 1 to 2 hours, and then the mixture was loaded onto a Superose 6 Increase 3.2/300 (GE Healthcare) equilibrated with the elution buffer [20 mM Hepes-NaOH (pH 7.4), 150 mM NaCl, 2 mM DTT] with 0.05% digitonin. Peak fractions were collected and analyzed by SDS-PAGE. His-sumo-Ypt32 with C-terminal truncation in various lengths were prepared as above and analyzed by SDS-PAGE.

Cryo-EM sample preparation and processing

Aliquots (~4 μl) of the TRAPPII complex (~1.5 mg/ml) or the TRAPPII-Ypt32 complex (~1.7 mg/ml) were applied to freshly glow-discharged holey carbon grids (Quantifoil Au R1.2/1.3 400 mesh) and blotted for 3.5 s in 100% humidity at 8°C. The grids were plunged into liquid ethane with Mark IV Vitrobot (FEI). Raw micrographs of the TRAPPII complex were collected using a Titan Krios microscope (Thermo Fisher Scientific) operated at 300 kV and equipped with a K2 Summit direct electron detector (Gatan) and a GIF Quantum energy filter (Gatan). The cryo-EM images were automatically collected using AutoEMation (53) with a slit width of 20 eV on the energy filter and a preset defocus range of −1.8 to −1.3 μm in super-resolution mode at a nominal magnification of ×105,000. A total dose of approximately 50 electrons per Å^{-2} for each movie stack was fracted into 32 frames over 5.6-s exposure time. The stacks were motion-corrected with MotionCor2 (54) and binned twofold, resulting in a pixel size of 1.091 Å. Raw micrographs of the TRAPPII-Ypt32 complex were collected using the same microscope (FEI) equipped with a K3 Summit direct electron detector (Gatan). The cryo-EM images were automatically collected using AutoEMation with a slit width of 20 eV on the energy filter and a preset defocus range of −1.8 to −1.3 μm in super-resolution mode at a nominal magnification of ×81,000. A total dose of approximately 50 electrons per Å^{-2} for each movie stack was fracted into 32 frames over 2.56-s exposure time. The stacks were motion-corrected with MotionCor2 and binned twofold, resulting in a pixel size of 0.8697 Å.

Image processing

Nearly all steps of image processing were performed using RELION (55–57). Contrast transfer function (CTF) parameters were estimated by CTFFIND4 (58). For the TRAPPII complex, we first manually picked and extracted about 2000 particles, which were applied to the reference-free 2D classification. The obtained class averages were used as templates for automatic particle picking in RELION. All autopicked particles were subjected to several rounds of 2D classification to remove obvious poor particles including ice contaminants and aggregates and further checked manually, after which a set of 809,002 particles was retained. A total of 2400 particles from 2D classification were selected to generate an initial model using RELION, which was low pass–filtered to 60 Å to be used as the template for 3D classification. After two rounds of 3D classification, 178,627 particles were selected and produced a 3D reconstruction with an average resolution of 3.87 Å without imposing any symmetry. A local mask of center region was applied during the refinement and improved the resolution to 3.46 Å (fig. S1E). The density map showed an apparent twofold symmetry, but only one-half displayed clear density and the other half exhibited very poor density, suggesting its heterogeneity. We used symmetry expansion to deal with this (32, 33). This approach is developed by S. H. W. Scheres, the developer of RELION software. The developer first used this approach (called symmetry expansion) to solve the structure of a human apoptosome complex that has a pseudo-symmetric C7 point group in 2015 (32) and later detailed it in the article "Processing of structurally heterogeneous cryo-EM data in RELION" of *Methods in Enzymology* in 2016 (33). Since then, this method has been widely used to deal with pseudo-symmetric complexes with heterogeneity. For example, the recently work published by Kudryashev and colleagues in *Nature Communications* reported the application of symmetry expansion to deal with the homopentameric 5-HT3A serotonin receptor that has a C5 pseudo-symmetry axis (59). By the symmetry expansion approach, they observed five different monomer conformations (59). Therefore, we think that this approach is effective for the conformational classification of the heterogeneous structure and could not result in a mistake. For our case, first, we expanded the dataset by rotating one monomer (half of the entire dimer) 180° along the C2 symmetry axis by adding 180 to the value of the column _rlnAngleRot in the star file of particles so that both monomers are reoriented onto a single position. We then performed classification by applying an extraordinarily soft mask around the reoriented monomers. The mask was created by relion_mask_create with the --ini_threshold set to 0.003, --extend_inimask set to 3, and --width_soft_edge set to 10. Through this strategy, two distinct conformations of monomer were identified, and 3D refinement yielded the open and closed structures at 4.18- and 3.79-Å resolutions, respectively (fig. S1F). We further assigned each monomer back to its original dimeric particle, resulting in the reconstruction of TRAPPII structure in three different states at resolutions of 4.36, 4.67, and 6.54 Å for states I, II, and III, respectively (fig. S1F). Local resolution was estimated by ResMap (60).

For the TRAPPII-Ypt32 complex, particles were automatically picked up using the same templates as TRAPPII in RELION. After 2D classification, all particles were checked manually and resulted in a set of 162,668 particles. After 3D classification, 56,658 particles were selected. Using the same expanded symmetry 3D classification strategy, we obtained one stable conformation of monomer at 3.80 Å (fig. S8B). By assigning each monomer back to its original dimeric particle, the whole structure of the TRAPPII-Ypt32 complex was resolved at 4.31 Å with imposing C2 symmetry (fig. S8B). Local masks of different subunits were applied to improve the quality of map density for model building.

Model building

The density maps of the TRAPPII monomer in different conformations and the TRAPPII-Ypt32 complex were used for the model building. The atomic models were generated by a strategy combining rigid body fitting, homology modeling, and de novo modeling.

Briefly, the crystal structures of core TRAPP/TRAPPI subcomplexes (PDB: 3CUE, 2J3T, and 2J3U) and Tca17 (PDB: 3PR6) were docked into the map using CHIMERA (*61*), and then the structure was manually rebuilt and adjusted on the basis of the density map in Coot (*62*). Atomic models of Trs65, Trs120, and Trs130 were built de novo. The results of MS analysis of the cross-linked TRAPPII complex provided hints for identifying those three important components. Secondary structure prediction by Phyre2 (*63*) aided the main-chain tracing. After poly-Ala backbones were built manually, different domains were searched by DALI server (*64*) to find ideal homolog models. Sequence assignments were guided mainly by bulky residues such as Trp, Tyr, Phe, Arg, and Lys. Models were refined using phenix.real_space_refinement against masked map by applying secondary structure restraints and stereochemical constraints (*65*). In case of possible clashes between different domains, combine_focused_map in Phenix was used (*65*). Last, most residues were assigned for all subunits with some residues were presented as poly-Ala. Residues 1 to 211 of Trs65, 1 to 263 of Trs120, 1 to 249 of Trs130, and 674 to 693 and 704 to 728 of Trs120 could not be modeled due to the poor density maps. For the TRAPPII-Ypt32 complex, Ypt32 in GDP/GTP form (PDB: 3RWM and 3RWO) and TRAPPII of closed conformation were docked into the map and manually rebuilt and adjusted in Coot. The final atomic models of TRAPPII in closed conformation and open conformation and the TRAPPII-Ypt32 monomer were cross-validated according to previously described procedures (*66, 67*). Briefly, atoms in the model were randomly shifted by up to 0.5 Å and then refined against one of the two independent half maps generated during the final 3D reconstruction. Then, the refined model was tested against the other map. To obtain the atomic models of the intact TRAPPII and TRAPPII-Ypt32 complex, atomic models of monomers were docked into the density maps of the dimeric TRAPPII in different states and the dimeric TRAPPII-Ypt32 complex. The data collection, model refinement, and validation statistics are presented in table S1. The model building is summarized in table S2. The statistics of the geometries of the models were generated using MolProbity (*68*). The sequence alignments were performed by Clustal W (*69*) and created by ESPript (*70*). All figures and movies were prepared using CHIMERA or PYMOL (www.pymol.org).

Chemical CXMS analysis

Following procedures previously described in (*71*), we performed CXMS analysis. About 10 μg of TRAPPII was cross-linked with 1 mM DSS or BS^3 for 1 hour at 25°C, and about 10 μg of the TRAPPII-Ypt32 complex was cross-linked with 1 mM DSS for 1 hour at 25°C. The reactions were quenched with 20 mM NH_4HCO_3. Proteins were precipitated with ice-cold acetone, resuspended in 8 M urea and 100 mM tris (pH 8.5), and then digested by trypsin (Promega) in 2 M urea and 100 mM tris (pH 8.5). The liquid chromatography–MS/MS analysis was performed on an Easy-nLC 1000 II HPLC (Thermo Fisher Scientific) coupled to a Q-Exactive HF mass spectrometer (Thermo Fisher Scientific). Peptides were loaded on a precolumn [75 μm inside diameter (ID), 6 cm long, packed with ODS-AQ 120 Å, 10-μm beads from YMC Co. Ltd.] and further separated on an analytical column (75 μm ID, 13 cm long, packed with Luna C18 1.9 μm, 100-Å resin from Welch Materials) with a linear reversed-phase gradient from 100% buffer A (0.1% formic acid in H_2O) to 30% buffer B (0.1% formic acid in acetonitrile) for 56 min at a flow rate of 200 nl/min. The top 15 most intense precursor ions from each full scan (resolution, 60,000) were isolated for HCD (higher energy collision dissociation) MS2 (resolution, 15,000; normalized collision energy, 27) with a dynamic exclusion time of 30 s. Precursors with 1+, 2+, 7+ or above, or unassigned charge states were excluded. The pLink (*72*) software was used to identify cross-linked peptides with precursor mass accuracy at 20 ppm and fragment ion mass accuracy at 20 ppm, and the results were filtered by applying a 5% false discovery rate cutoff at the spectral level and then an *E* value cutoff at 0.001 (*73*).

Antibody labeling

A yeast strain, in which Trs65 gene was deleted from the genome and contained C-terminal 3xFlag-tagged Trs120, was constructed and named Trs65del.

The construction of 6xHIS-GFP-Trs65 driven by GAL1 promotor was transformed into yeast strain Trs65del. Twelve liters of transformed yeast cells was cultured in minimal medium lacking leucine with supplement of raffinose until the OD_{600} reached logarithmic growth phase, and then galactose was added to the final concentration of 100 mM. After 6 hours of culture, the cells were pelleted and proteins were purified by anti-Flag affinity resins (Sigma-Aldrich). Anti-HIS antibodies (ZSGB-BIO) were added at a 1:1.5 molar ratio (antibody to protein) into the purified protein and incubated for 30 min at room temperature. The sample was concentrated and applied to Superose 6 Increase 3.2/300 (GE Healthcare). The peak fraction was analyzed by negative-stain EM.

Dilution plating assays

Yeast strains with N-terminal or C-terminal truncation of Trs120 or Trs130 were produced via plasmid shuffling. *TRS120* and *TRS130* were separately constructed into P414/P416 plasmid under the control of the alcohol dehydrogenase (ADH) promoter and the CYC1 terminator. The chromosomal genes *TRS120* and *TRS130* were disrupted with a *HIS3* cassette. For growth analysis, cells were grown at 30°C, then washed by sterilized water, and diluted to OD_{600} of 1.25. The cells were plated at fivefold serial dilutions on SC-HIS/TRP [synthetic complete supplement mixture (SC) without L-Histidine or L-Tryptophan] plates with or without 5-FOA (5-fluoroorotic acid) at 25°, 30°, and 37°C for 72 hours. Three independent experiments were performed, and one representative is presented in the figure.

Spotting assay quantification

Spotting assays were quantified by ImageJ, as described in the protocol (*74*). All acquired agar plate images were preprocessed by background subtraction to ensure uniformity, and then the appropriate third dilution was chosen for quantification. Using the same circle selection tool, we measured the gray values of background and each spot in third dilution under different temperature conditions for three times. Images of two independent biological replicates were used for quantification, and the raw values were recorded and normalized to a control on the same plate. Statistical analysis was performed using a one-way analysis of variance (ANOVA), followed by Tukey's test with a 95% confidence interval in Origin 8.0.

SUPPLEMENTARY MATERIALS

Supplementary material for this article is available at https://science.org/doi/10.1126/sciadv.abi5603

View/request a protocol for this paper from *Bio-protocol*.

REFERENCES AND NOTES

1. J. S. Bonifacino, B. S. Glick, The mechanisms of vesicle budding and fusion. *Cell* **116**, 153–166 (2004).

2. H. Cai, K. Reinisch, S. Ferro-Novick, Coats, tethers, Rabs, and SNAREs work together to mediate the intracellular destination of a transport vesicle. *Dev. Cell* **12**, 671–682 (2007).

3. J. Shorter, M. B. Beard, J. Seemann, A. B. Dirac-Svejstrup, G. Warren, Sequential tethering of Golgins and catalysis of SNAREpin assembly by the vesicle-tethering protein p115. *J. Cell Biol.* **157**, 45–62 (2002).

4. A. H. Hutagalung, P. J. Novick, Role of Rab GTPases in membrane traffic and cell physiology. *Physiol. Rev.* **91**, 119–149 (2011).

5. H. Cai, S. Yu, S. Menon, Y. Cai, D. Lazarova, C. Fu, K. Reinisch, J. C. Hay, S. Ferro-Novick, TRAPPI tethers COPII vesicles by binding the coat subunit Sec23. *Nature* **445**, 941–944 (2007).

6. A. Yamasaki, S. Menon, S. Yu, J. Barrowman, T. Meerloo, V. Oorschot, J. Klumperman, A. Satoh, S. Ferro-Novick, mTrs130 is a component of a mammalian TRAPPII complex, a Rab1 GEF that binds to COPI-coated vesicles. *Mol. Biol. Cell* **20**, 4205–4215 (2009).

7. H. Stenmark, Rab GTPases as coordinators of vesicle traffic. *Nat. Rev. Mol. Cell Biol.* **10**, 513–525 (2009).

8. J. J. Kim, Z. Lipatova, N. Segev, TRAPP complexes in secretion and autophagy. *Front. Cell Dev. Biol.* **4**, 20 (2016).

9. M. Sacher, Y. Jiang, J. Barrowman, A. Scarpa, J. Burston, L. Zhang, D. Schieltz, J. R. Yates III, H. Abeliovich, S. Ferro-Novick, TRAPP, a highly conserved novel complex on the cis-Golgi that mediates vesicle docking and fusion. *EMBO J.* **17**, 2494–2503 (1998).

10. H. Cai, Y. Zhang, M. Pypaert, L. Walker, S. Ferro-Novick, Mutants in trs120 disrupt traffic from the early endosome to the late Golgi. *J. Cell Biol.* **171**, 823–833 (2005).

11. N. Morozova, Y. Liang, A. A. Tokarev, S. H. Chen, R. Cox, J. Andrejic, Z. Lipatova, V. A. Sciorra, S. D. Emr, N. Segev, TRAPPII subunits are required for the specificity switch of a Ypt-Rab GEF. *Nat. Cell Biol.* **8**, 1263–1269 (2006).

12. D. Tan, Y. Cai, J. Wang, J. Zhang, S. Menon, H. T. Chou, S. Ferro-Novick, K. M. Reinisch, T. Walz, The EM structure of the TRAPPIII complex leads to the identification of a requirement for COPII vesicles on the macroautophagy pathway. *Proc. Natl. Acad. Sci. U.S.A.* **110**, 19432–19437 (2013).

13. J. Barrowman, D. Bhandari, K. Reinisch, S. Ferro-Novick, TRAPP complexes in membrane traffic: Convergence through a common Rab. *Nat. Rev. Mol. Cell Biol.* **11**, 759–763 (2010).

14. C. Choi, M. Davey, C. Schluter, P. Pandher, Y. Fang, L. J. Foster, E. Conibear, Organization and assembly of the TRAPPII complex. *Traffic* **12**, 715–725 (2011).

15. M. A. Lynch-Day, D. Bhandari, S. Menon, J. Huang, H. Cai, C. R. Bartholomew, J. H. Brumell, S. Ferro-Novick, D. J. Klionsky, Trs85 directs a Ypt1 GEF, TRAPPIII, to the phagophore to promote autophagy. *Proc. Natl. Acad. Sci. U.S.A.* **107**, 7811–7816 (2010).

16. M. Pinar, E. Arias-Palomo, V. de los Rios, H. N. Arst Jr., M. A. Penalva, Characterization of *Aspergillus nidulans* TRAPPs uncovers unprecedented similarities between fungi and metazoans and reveals the modular assembly of TRAPPII. *PLOS Genet.* **15**, e1008557 (2019).

17. F. Riedel, A. Galindo, N. Muschalik, S. Munro, The two TRAPP complexes of metazoans have distinct roles and act on different Rab GTPases. *J. Cell Biol.* **217**, 601–617 (2018).

18. A. Galindo, V. J. Planelles-Herrero, G. Degliesposti, S. Munro, Cryo-EM structure of metazoan TRAPPIII, the multi-subunit complex that activates the GTPase Rab1. *EMBO J.* **40**, e107608 (2021).

19. L. L. Thomas, A. M. N. Joiner, J. C. Fromme, The TRAPPIII complex activates the GTPase Ypt1 (Rab1) in the secretory pathway. *J. Cell Biol.* **217**, 283–298 (2018).

20. W. Wang, M. Sacher, S. Ferro-Novick, TRAPP stimulates guanine nucleotide exchange on Ypt1p. *J. Cell Biol.* **151**, 289–296 (2000).

21. S. Jones, C. Newman, F. Liu, N. Segev, The TRAPP complex is a nucleotide exchanger for Ypt1 and Ypt31/32. *Mol. Biol. Cell* **11**, 4403–4411 (2000).

22. M. Pinar, H. N. Arst Jr., A. Pantazopoulou, V. G. Tagua, V. de los Ríos, J. Rodríguez-Salarichs, J. F. Díaz, M. A. Peñalva, TRAPPII regulates exocytic Golgi exit by mediating nucleotide exchange on the Ypt31 ortholog RabERAB11. *Proc. Natl. Acad. Sci. U.S.A.* **112**, 4346–4351 (2015).

23. C. J. Zhang, J. Bradford Bowzard, A. Greene, A. Anido, K. Stearns, R. A. Kahn, Genetic interactions link ARF1, YPT31/32 and TRS130. *Yeast* **19**, 1075–1086 (2002).

24. A. Pantazopoulou, M. Pinar, X. Xiang, M. A. Penalva, Maturation of late Golgi cisternae into RabE(RAB11) exocytic post-Golgi carriers visualized in vivo. *Mol. Biol. Cell* **25**, 2428–2443 (2014).

25. Y.-G. Kim, S. Raunser, C. Munger, J. Wagner, Y. L. Song, M. Cygler, T. Walz, B. H. Oh, M. Sacher, The architecture of the multisubunit TRAPP I complex suggests a model for vesicle tethering. *Cell* **127**, 817–830 (2006).

26. Y. Cai, H. F. Chin, D. Lazarova, S. Menon, C. Fu, H. Cai, A. Sclafani, D. W. Rodgers, E. M. de la Cruz, S. Ferro-Novick, K. M. Reinisch, The structural basis for activation of the Rab Ypt1p by the TRAPP membrane-tethering complexes. *Cell* **133**, 1202–1213 (2008).

27. C. K. Yip, J. Berscheminski, T. Walz, Molecular architecture of the TRAPPII complex and implications for vesicle tethering. *Nat. Struct. Mol. Biol.* **17**, 1298–1304 (2010).

28. L. L. Thomas, J. C. Fromme, GTPase cross talk regulates TRAPPII activation of Rab11 homologues during vesicle biogenesis. *J. Cell Biol.* **215**, 499–513 (2016).

29. W. Wang, S. Ferro-Novick, A Ypt32p exchange factor is a putative effector of Ypt1p. *Mol. Biol. Cell* **13**, 3336–3343 (2002).

30. Y. Liang, N. Morozova, A. A. Tokarev, J. W. Mulholland, N. Segev, The role of Trs65 in the Ypt/Rab guanine nucleotide exchange factor function of the TRAPP II complex. *Mol. Biol. Cell* **18**, 2533–2541 (2007).

31. B. Montpetit, E. Conibear, Identification of the novel TRAPP associated protein Tca17. *Traffic* **10**, 713–723 (2009).

32. M. Zhou, Y. Li, Q. Hu, X. C. Bai, W. Huang, C. Yan, S. H. W. Scheres, Y. Shi, Atomic structure of the apoptosome: Mechanism of cytochrome c- and dATP-mediated activation of Apaf-1. *Genes Dev.* **29**, 2349–2361 (2015).

33. S. H. Scheres, Processing of structurally heterogeneous cryo-EM data in RELION. *Methods Enzymol.* **579**, 125–157 (2016).

34. D. Taussig, Z. Lipatova, J. J. Kim, X. Zhang, N. Segev, Trs20 is required for TRAPP II assembly. *Traffic* **14**, 678–690 (2013).

35. M. Sacher, N. Shahrzad, H. Kamel, M. P. Milev, TRAPPopathies: An emerging set of disorders linked to variations in the genes encoding transport protein particle (TRAPP)-associated proteins. *Traffic* **20**, 5–26 (2019).

36. A. K. Gedeon, G. E. Tiller, M. le Merrer, S. Heuertz, L. Tranebjaerg, D. Chitayat, S. Robertson, I. A. Glass, R. Savarirayan, W. G. Cole, D. L. Rimoin, B. G. Kousseff, H. Ohashi, B. Zabel, A. Munnich, J. Gecz, J. C. Mulley, The molecular basis of X-linked spondyloepiphyseal dysplasia tarda. *Am. J. Hum. Genet.* **68**, 1386–1397 (2001).

37. M. Zong, X. G. Wu, C. W. L. Chan, M. Y. Choi, H. C. Chan, J. A. Tanner, S. Yu, The adaptor function of TRAPPC2 in mammalian TRAPPs explains TRAPPC2-associated SEDT and TRAPPC9-associated congenital intellectual disability. *PLOS ONE* **6**, e23350 (2011).

38. A. M. Joiner, B. P. Phillips, K. Yugandhar, E. J. Sanford, M. B. Smolka, H. Yu, E. A. Miller, J. C. Fromme, Structural basis of TRAPPIII-mediated Rab1 activation. *EMBO J.* **40**, e107607 (2021).

39. L. L. Thomas, S. A. van der Vegt, J. C. Fromme, A steric gating mechanism dictates the substrate specificity of a Rab-GEF. *Dev. Cell* **48**, 100–114.e9 (2019).

40. A. Sultana, Y. Jin, C. Dregger, E. Franklin, L. S. Weisman, A. R. Khan, The activation cycle of Rab GTPase Ypt32 reveals structural determinants of effector recruitment and GDI binding. *FEBS Lett.* **585**, 3520–3527 (2011).

41. A. Itzen, R. S. Goody, GTPases involved in vesicular trafficking: Structures and mechanisms. *Semin. Cell Dev. Biol.* **22**, 48–56 (2011).

42. V. Hauryliuk, S. Hansson, M. Ehrenberg, Cofactor dependent conformational switching of GTPases. *Biophys. J.* **95**, 1704–1715 (2008).

43. A. Valencia, P. Chardin, A. Wittinghofer, C. Sander, The ras protein family: Evolutionary tree and role of conserved amino acids. *Biochemistry* **30**, 4637–4648 (1991).

44. B. L. Grosshans, D. Ortiz, P. Novick, Rabs and their effectors: Achieving specificity in membrane traffic. *Proc. Natl. Acad. Sci. U.S.A.* **103**, 11821–11827 (2006).

45. O. Pylypenko, A. Rak, T. Durek, S. Kushnir, B. E. Dursina, N. H. Thomae, A. T. Constantinescu, L. Brunsveld, A. Watzke, H. Waldmann, R. S. Goody, K. Alexandrov, Structure of doubly prenylated Ypt1:GDI complex and the mechanism of GDI-mediated Rab recycling. *EMBO J.* **25**, 13–23 (2006).

46. A. Ignatev, S. Kravchenko, A. Rak, R. S. Goody, O. Pylypenko, A structural model of the GDP dissociation inhibitor rab membrane extraction mechanism. *J. Biol. Chem.* **283**, 18377–18384 (2008).

47. M. Sacher, J. Barrowman, D. Schieltz, J. R. Yates III, S. Ferro-Novick, Identification and characterization of five new subunits of TRAPP. *Eur. J. Cell Biol.* **79**, 71–80 (2000).

48. A. A. Tokarev, D. Taussig, G. Sundaram, Z. Lipatova, Y. Liang, J. W. Mulholland, N. Segev, TRAPP II complex assembly requires Trs33 or Trs65. *Traffic* **10**, 1831–1844 (2009).

49. J. L. Brown, Z. Kossaczka, B. Jiang, H. Bussey, A mutational analysis of killer toxin resistance in Saccharomyces cerevisiae identifies new genes involved in cell wall (1-->6)-beta-glucan synthesis. *Genetics* **133**, 837–849 (1993).

50. L. Fernandez-Ricaud, J. Warringer, E. Ericson, K. Glaab, P. Davidsson, F. Nilsson, G. J. L. Kemp, O. Nerman, A. Blomberg, PROPHECY—A yeast phenome database, update 2006. *Nucleic Acids Res.* **35**, D463–D467 (2007).

51. M. Pinar, M. A. Peñalva, *En bloc* TGN recruitment of *Aspergillus* TRAPPII reveals TRAPP maturation as unlikely to drive RAB1-to-RAB11 transition. *J. Cell Sci.* **133**, jcs241141 (2020).

52. M. S. Longtine, A. Mckenzie III, D. J. Demarini, N. G. Shah, A. Wach, A. Brachat, P. Philippsen, J. R. Pringle, Additional modules for versatile and economical PCR-based gene deletion and modification in Saccharomyces cerevisiae. *Yeast* **14**, 953–961 (1998).

53. J. Lei, J. Frank, Automated acquisition of cryo-electron micrographs for single particle reconstruction on an FEI Tecnai electron microscope. *J. Struct. Biol.* **150**, 69–80 (2005).

54. S. Q. Zheng, E. Palovcak, J. P. Armache, K. A. Verba, Y. Cheng, D. A. Agard, MotionCor2: Anisotropic correction of beam-induced motion for improved cryo-electron microscopy. *Nat. Methods* **14**, 331–332 (2017).

55. S. H. Scheres, RELION: Implementation of a Bayesian approach to cryo-EM structure determination. *J. Struct. Biol.* **180**, 519–530 (2012).

56. J. Zivanov, T. Nakane, B. O. Forsberg, D. Kimanius, W. J. H. Hagen, E. Lindahl, S. H. W. Scheres, New tools for automated high-resolution cryo-EM structure determination in RELION-3. *eLife* **7**, (2018).

57. D. Kimanius, B. O. Forsberg, S. H. Scheres, E. Lindahl, Accelerated cryo-EM structure determination with parallelisation using GPUs in RELION-2. *eLife* **5**, (2016).

58. H. Elmlund, D. Elmlund, S. Bengio, PRIME: Probabilistic initial 3D model generation for single-particle cryo-electron microscopy. *Structure* **21**, 1299–1306 (2013).

59. Y. Zhang, P. M. Dijkman, R. Zou, M. Zandl-Lang, R. M. Sanchez, L. Eckhardt-Strelau, H. Köfeler, H. Vogel, S. Yuan, M. Kudryashev, Asymmetric opening of the homopentameric 5-HT3A serotonin receptor in lipid bilayers. *Nat. Commun.* **12**, 1074 (2021).

60. A. Kucukelbir, F. J. Sigworth, H. D. Tagare, Quantifying the local resolution of cryo-EM density maps. *Nat. Methods* **11**, 63–65 (2014).

61. E. F. Pettersen, T. D. Goddard, C. C. Huang, G. S. Couch, D. M. Greenblatt, E. C. Meng, T. E. Ferrin, UCSF chimera - A visualization system for exploratory research and analysis. *J. Comput. Chem.* **25**, 1605–1612 (2004).

62. P. Emsley, B. Lohkamp, W. G. Scott, K. Cowtan, Features and development of Coot. *Acta Crystallogr. D Biol. Crystallogr.* **66**, 486–501 (2010).

63. L. A. Kelley, S. Mezulis, C. M. Yates, M. N. Wass, M. J. E. Sternberg, The Phyre2 web portal for protein modeling, prediction and analysis. *Nat. Protoc.* **10**, 845–858 (2015).

64. L. Holm, DALI and the persistence of protein shape. *Protein Sci.* **29**, 128–140 (2020).

65. P. D. Adams, P. V. Afonine, G. Bunkóczi, V. B. Chen, I. W. Davis, N. Echols, J. J. Headd, L. W. Hung, G. J. Kapral, R. W. Grosse-Kunstleve, A. J. McCoy, N. W. Moriarty, R. Oeffner, R. J. Read, D. C. Richardson, J. S. Richardson, T. C. Terwilliger, P. H. Zwart, PHENIX: A comprehensive Python-based system for macromolecular structure solution. *Acta Crystallogr. D Biol. Crystallogr.* **66**, 213–221 (2010).

66. P. V. Afonine, B. P. Klaholz, N. W. Moriarty, B. K. Poon, O. V. Sobolev, T. C. Terwilliger, P. D. Adams, A. Urzhumtsev, New tools for the analysis and validation of cryo-EM maps and atomic models. *Acta Crystallogr. D Struct. Biol.* **74**, 814–840 (2018).

67. A. Amunts, A. Brown, X. C. Bai, J. L. Llácer, T. Hussain, P. Emsley, F. Long, G. Murshudov, S. H. W. Scheres, V. Ramakrishnan, Structure of the yeast mitochondrial large ribosomal subunit. *Science* **343**, 1485–1489 (2014).

68. C. J. Williams, J. J. Headd, N. W. Moriarty, M. G. Prisant, L. L. Videau, L. N. Deis, V. Verma, D. A. Keedy, B. J. Hintze, V. B. Chen, S. Jain, S. M. Lewis, W. B. Arendall III, J. Snoeyink, P. D. Adams, S. C. Lovell, J. S. Richardson, D. C. Richardson, MolProbity: More and better reference data for improved all-atom structure validation. *Protein Sci.* **27**, 293–315 (2018).

69. M. A. Larkin, G. Blackshields, N. P. Brown, R. Chenna, P. A. McGettigan, H. McWilliam, F. Valentin, I. M. Wallace, A. Wilm, R. Lopez, J. D. Thompson, T. J. Gibson, D. G. Higgins, Clustal W and Clustal X version 2.0. *Bioinformatics* **23**, 2947–2948 (2007).

70. X. Robert, P. Gouet, Deciphering key features in protein structures with the new ENDscript server. *Nucleic Acids Res.* **42**, W320–W324 (2014).

71. K. Mei, Y. Li, S. Wang, G. Shao, J. Wang, Y. Ding, G. Luo, P. Yue, J. J. Liu, X. Wang, M. Q. Dong, H. W. Wang, W. Guo, Cryo-EM structure of the exocyst complex. *Nat. Struct. Mol. Biol.* **25**, 139–146 (2018).

72. Z. L. Chen, J. M. Meng, Y. Cao, J. L. Yin, R. Q. Fang, S. B. Fan, C. Liu, W. F. Zeng, Y. H. Ding, D. Tan, L. Wu, W. J. Zhou, H. Chi, R. X. Sun, M. Q. Dong, S. M. He, A high-speed search engine pLink 2 with systematic evaluation for proteome-scale identification of cross-linked peptides. *Nat. Commun.* **10**, 3404 (2019).

73. B. Yang, Y. J. Wu, M. Zhu, S. B. Fan, J. Lin, K. Zhang, S. Li, H. Chi, Y. X. Li, H. F. Chen, S. K. Luo, Y. H. Ding, L. H. Wang, Z. Hao, L. Y. Xiu, S. Chen, K. Ye, S. M. He, M. Q. Dong, Identification of cross-linked peptides from complex samples. *Nat. Methods* **9**, 904–906 (2012).

74. A. A. Petropavlovskiy, M. G. Tauro, P. Lajoie, M. L. Duennwald, A quantitative imaging-based protocol for yeast growth and survival on agar plates. *STAR Protoc.* **1**, 100182 (2020).